

# Optimizing orbital debris monitoring with optical telescopes

James R. Shell

US Air Force, Space Innovation and Development Center  
24 Talon Way, Schriever AFB, CO 80912

## ABSTRACT

Continued growth in the orbital debris population has renewed concerns over the long-term use of space. Debris poses an increasing risk to manned space missions and operational satellites; however, the majority of debris large enough to cause catastrophic damage is not being tracked and maintained in a catalog. Passive optical systems hold great promise to provide a cost-effective means to monitor orbital debris. Recent advances in optical system design, detectors and image processing have enabled new capabilities. This work examines the performance of optical systems operating in a fixed or non-tracking mode for uncued debris detection. The governing radiometric equations for sensing orbital debris are developed, illustrating the performance dependencies according to the telescope optics, detector, atmosphere and debris properties. The governing equations are exercised by examining three debris monitoring scenarios: commonly used ground-based systems monitoring the geosynchronous orbit (GEO), a novel approach for using ground-based telescopes to monitor low earth orbit (LEO), and finally systems such as star trackers and small cameras hosted on GEO-based satellites for monitoring GEO. Performance analysis indicates significant potential contributions of these systems as a cost-effective means for monitoring the growing debris population—this is particularly true for small aperture ground-based telescopes for monitoring LEO and GEO-based sensors monitoring GEO.

**Keywords:** Orbital debris, telescopes

## 1. INTRODUCTION

The growing orbital debris population has renewed concerns over the long term-viability of the space environment and the resulting economic impacts. The 2007 China anti-satellite test and the 2009 collision between the defunct *Cosmos 2251* and the operational *Iridium 33* satellites have significantly expanded the LEO debris population. These two events alone have doubled the number of fragmentation objects, producing 250,000 new pieces of debris one centimeter and larger, expanding this population to ~500,000 objects.<sup>1</sup> Debris in the geosynchronous orbit (GEO) environment has also continued to increase, and although the spatial densities in this regime aren't as high as those in LEO, the uniqueness of mission-enabling geostationary orbits prompts an increased scrutiny of GEO debris. Current NASA estimates indicate there are approximately 3250 GEO debris objects 10 cm and larger.<sup>2, 3</sup>

The U.S. Space Surveillance Network (SSN)<sup>4</sup> tracks satellites and space debris, all generically termed “resident space objects” (RSOs) with some 21,000 objects being monitored as of June 2010. Of this population, only around 1000 are active satellites.<sup>5</sup> Sensitivity limitations result in minimum debris sizes which are maintained in the space catalog, generally around 10 cm for LEO objects and 70 cm for GEO objects.<sup>6</sup> However, impacts from debris as small as 1 cm in LEO may result in mission-ending satellite failures. RSOs smaller than those maintained in the catalog may be detected and their populations statistically sampled, but the orbital positions are not maintained due to inadequate sensor coverage.

The United States National Space Policy released in 2010 addresses space debris and has identified debris monitoring and awareness as an area for potential international cooperation.<sup>7</sup> Likewise, the United Nations Committee on Peaceful Uses of Outer Space has continued to urge international cooperation.<sup>8</sup> Application of optical systems may help satisfy these needs due to advancements in commercial components enabling improved performance from hardware with relatively low costs, as compared with traditional space surveillance sensors. This work focuses on applying these commercial technologies with telescopes used in “survey” mode, where the pointing is fixed and objects pass through the field of view.

First, orbital debris properties are discussed, to include sizes, distributions, and optical signatures. The governing radiometric equations are established, providing a framework enabling the parametric investigation of design parameters and conditions optimal for debris monitoring. Three specific scenarios are examined: the traditional use of ground-based telescopes monitoring GEO RSOs, a novel application of small aperture ground-based telescopes for monitoring LEO RSOs, and finally, the use of small cameras in GEO, such as star trackers, to monitor GEO-based RSOs.

## 2. ORBITAL DEBRIS OPTICAL SIGNATURES

We desire to understand orbital debris optical signatures in order to estimate the efficacy of passive sensing approaches. These signatures are based to first order on the RSO sizes and optical properties. For the LEO regime, the small size debris population is estimated based on radar debris surveys in a “beam park” mode.<sup>9</sup> Similarly, GEO debris population estimates are made using debris surveys conducted by ground-based telescopes.<sup>10</sup> In this manner, a statistical understanding of the debris population as a function of size and orbital characteristics is obtained.

The true nature of the signature to size relationship is fraught with uncertainty. Several techniques have been used to estimate debris optical reflectance or albedo values. Many rely upon the cross-correlation of apparent sizes as measured by a complementary phenomenology such as radar<sup>11</sup> or thermal infrared.<sup>12</sup> The good news for optical sensors is that the estimated debris albedo has been revised upward, with recent work establishing a mean value of  $\rho = 0.175$  for fragmented space debris,<sup>13</sup> a revision from early 1990s estimates of 0.09-0.12.<sup>14</sup> An albedo of 0.2 is often used for payloads and rocket bodies.

The closed form solution for a signature calculation is complex, and is a function of many variables to include the object size; shape; orientation; the geometry of the observer, sun and object; and the bidirectional reflectance distribution function (BRDF)<sup>15</sup> of the materials. We will use a simple sphere to estimate debris optical signatures. By convention, optical signatures use the visual magnitude system, adopted from astronomers. The unitless and logarithmic magnitude system references the star of Vega as a zero point, resulting in the sun having a visual magnitude ( $m_{sun}$ ) of -26.73.

It may be shown that the signature of an object ( $m_{obj}$ ), when approximated as a sphere, is given by

$$m_{obj} = m_{sun} - 2.5 \log \left[ \frac{d^2}{R^2} \cdot \rho \cdot p(\psi) \right], \quad (1)$$

where  $d$  is the diameter of the object,  $R$  is the range to the object from the observer,  $\rho$  is the reflectance, and  $p(\psi)$  is the solar phase angle function. The solar phase angle,  $\psi$ , is the angular extent between the sun and the observer, relative to the object. For diffuse, or Lambertian, surfaces, the total reflected energy decreases with increasing phase angles as observed with the lunar phases. For specular or mirrored surfaces, there is no such dependency. Our estimates will assume equal contributions from both specular and diffuse reflectance components, which is supported by observational data. Finally, gray body reflectance will be considered for the objects, such that  $\rho$  is constant for all wavelengths.

For a sphere, the specular phase angle function is a constant  $1/4$ , while the diffuse phase angle function is given by

$$p_{diff}(\psi) = \frac{2}{3\pi} \cdot [\sin(\psi) + (\pi - \psi)\cos(\psi)].^{16} \quad (2)$$

The signature of a spherical object using both specular and diffuse components then becomes

$$m_{obj} = m_{sun} - 2.5 \log \left[ \frac{d^2}{R^2} \cdot \left( \frac{\rho_{spec}}{4} + \rho_{diff} p_{diff}(\psi) \right) \right]. \quad (3)$$

Visual magnitudes may have meaning relative to the brightness of astronomical objects, but do not enable a physics-based assessment of sensor performance. Absolute radiometric units are required, and it is ultimately the at-aperture irradiance in terms of power (Watts/area) or photon flux (photons/second/area) that is required to evaluate sensing performance. The conversion from visual magnitude to irradiance in terms of power per unit area is made according to

$$E_{RSO\_Power} = 1.78 \times 10^{-8} \cdot 10^{-0.4 m_{obj}} \text{ [W/m}^2\text{]}, \quad (4)$$

where it is noted that a zero-magnitude source provides an irradiance of  $1.78 \times 10^{-8} \text{ W/m}^2$  integrated over the typical spectral response of a silicon-based sensor. Since the sensors of interest are photon detecting CCDs, it is ultimately the photon-based irradiance that is needed. Conversion of visual magnitude to photon-based irradiance is accomplished by converting the zero magnitude power flux density into photon density via multiplication by  $(\lambda / h c)$  where  $h$  is Planck's constant,  $c$  is the speed of light and  $\lambda$  is the wavelength. Using a wavelength of 625 nm as a weighted average for a typical silicon sensor, the resulting photon irradiance ( $E_{RSO}$ ) as a function of visual magnitude is

$$E_{RSO} = 5.6 \times 10^{10} \cdot 10^{-0.4 m_{obj}} \text{ [ph/s/m}^2\text{]}. \quad (5)$$

For reference, 10 cm objects in LEO and 70 cm objects in GEO, or the approximate minimum sizes contained in the space catalog, corresponding to exoatmospheric signatures of 11.2  $m_v$  and 15.2  $m_v$ , respectively, or  $1.9 \times 10^6 \text{ ph/s/m}^2$  and  $4.5 \times 10^4 \text{ ph/s/m}^2$ .

### 3. RADIOMETRIC EQUATION DEVELOPMENT

With orbital debris signatures quantified, the governing radiometric equations are developed for optical sensing. The key components include the optical system properties, the detector performance, the background radiance, the RSO brightness and angular rate, and the atmospheric transmittance loss for ground-based sensors. The spectral range considered is limited to that covered by silicon detectors, or approximately 300-1100 nm. However, the governing equations are extensible over larger spectral ranges, as long as reflected solar energy dominates over the blackbody component.

The usual standoff distances over which RSOs are observed, coupled with their sizes results in a point source to the optical systems of interest. The typical scaling for these classes of telescopes is such that the pixel sizes are large compared to the point spread function. Furthermore, ground-based system resolution is limited by the atmospheric seeing conditions in all but the smallest of aperture sizes and/or pristine seeing conditions. For instance, a 15 cm aperture results in approximately a two arc second point spread function, similar to typical atmospheric seeing conditions. The same aperture with a focal ratio of two (or a 30 cm focal length) results in a diffraction-limited point spread function of  $\approx 1.5$  micron. The result is a focus spot size which is small compared to the pixel sizes, enabling an approximation that most of the energy for a point source falls within a single photo site on the detector.

#### 3.1 RSO Signal

Solar-reflected light from a debris object or RSO is first transmitted with an irradiance of  $E_{RSO}$  to an optical system having an aperture diameter of  $d$ . For ground-based sensing, there is a signal loss associated with the atmospheric transmittance,  $\tau_{atm}$ , which determines the fraction of energy successfully reaching the aperture. Upon reaching the aperture, additional losses are incurred before reaching the detector due to the finite optical transmittance ( $\tau$ ) to include obscurations by telescope secondaries if present. The resulting power or photon flux from the RSO, or the signal power ( $P_s$ ) on a single detector pixel is then given by

$$P_s = \tau \frac{\pi \cdot d^2}{4} \tau_{atm} E_{RSO} \text{ [ph/sec]}. \quad (6)$$

Once incident upon the detector, the photons are converted to signal photoelectrons ( $e_s$ ) according to the solar-weighted quantum efficiency ( $QE$ ) of the detector. Finally, the signal photoelectron rate is multiplied by the signal integration time,  $t_{sig}$ , to make the conversion to the total number of photoelectrons. The number of signal photoelectrons ( $e_s$ ) is therefore given by

$$e_s = QE \cdot \tau \cdot A \cdot \tau_{atm} \cdot E_{RSO} \cdot t_{sig} \text{ [photoelectrons]} \quad (7)$$

where  $A$  has replaced  $\pi \cdot d^2 / 4$  as the aperture area. The *signal* integration time of interest,  $t_{sig}$ , is generally not equal to the *system* integration time due the angular movement of the object during an exposure period. This highlights the fact that the maximum signal possible is that obtained when the RSO moves through the full length of a pixel during an exposure. Additional integration time only results in a streak on the focal plane, which allows more accumulation of the background energy, thus decreasing the signal to noise.

### 3.2 Background Radiance or Noise

The background radiance is responsible for providing the competing noise signal. For ground-based observations, this is dominated by Rayleigh-scattered sunlight during the day and twilight conditions for the spectral bands of interest. For a typical site, once nautical twilight conditions are reached, or the sun is 12° below the horizon, the dominant background effects include Rayleigh-scattered moonlight (if the moon is visible), local light pollution and upper atmospheric atomic recombination which dominates in the near infrared. Space-based sensors have the advantage of a reduced background compared to ground-based sensors, but it varies according to the stellar densities.

Background signatures are often provided in terms of visual magnitudes per arc second squared ( $m_v/\text{asec}^2$ ). As with RSO signatures, this background radiance specification must be converted to absolute radiometric units. Given a background of  $Mb$  in units of visual magnitudes per square arc second, the conversion to absolute radiometric units of photons per second per meter squared per steradian is given by

$$L_b = 5.6 \times 10^{10} \cdot 10^{-0.4 \cdot Mb} \cdot \left(\frac{180}{\pi}\right)^2 \cdot 3600^2, \quad [\text{ph}/\text{sec}/\text{m}^2/\text{sr}] \quad (8)$$

where, as before, the typical spectral response of a silicon-based detector is used.

This spatially-extended background radiance source provides an irradiance on the detector focal plane ( $E_{det}$ ) given by

$$E_{det} = \frac{\tau \cdot \pi \cdot L_b}{[1 + 4(f/d)^2]} \quad [\text{ph}/\text{sec}/\text{m}^2], \quad (9)$$

where the new variable  $f$  is the optical system focal length.<sup>17</sup> The same optical system transmittance losses associated with the RSO signal are also present in this case, and it is noted that the energy is driven by the  $f\#$  or  $d/f$  of the optical system. The per pixel background noise power is calculated by taking the product of the background irradiance on the focal plane with the area of a pixel. Only square pixels will be considered such that the background or noise photon incident rate ( $P_N$ ) on an individual pixel is

$$P_N = \frac{\tau \cdot \pi \cdot L_b}{[1 + 4(f/d)^2]} \cdot x^2 \quad [\text{ph}/\text{sec}], \quad (10)$$

where  $x$  is the pixel size. Figure 1 illustrates this rate over a range of pixel sizes and sky brightness values.

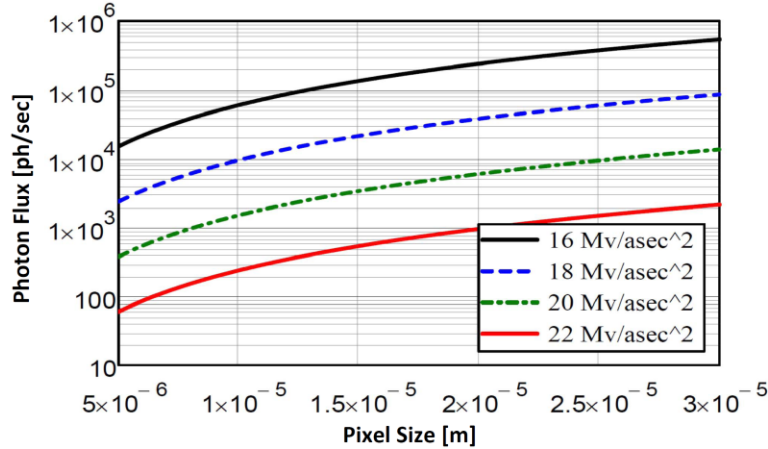


Figure 1 The background photon flux incident per pixel (y-axis) as a function of pixel size ranging from 5 to 30  $\mu\text{m}$  (x-axis) at varying background levels for an  $f/1.0$  system, with lossless transmittance (i.e.,  $f/d$  and  $\tau$  are equal to unity in Equation 10). Background levels of 22, 20, 18 and 16  $m_v/\text{asec}^2$  are shown in red, green, blue, and black, respectively.

Finally, the incident background photons are converted to photogenerated electrons ( $e_b$ ) by the same quantum efficiency ( $QE$ ) value for the signal photons, and integrated over time  $t$  to produce the total number of background-derived photoelectrons according to

$$e_b = QE \frac{\tau \cdot \pi \cdot L_b \cdot x^2}{[1 + 4(f/d)^2]} \cdot t \quad [\text{photoelectrons}]. \quad (11)$$

A simplification of the background noise equation is possible by approximating the  $1 + 4(f/d)^2$  denominator term as  $4(f/d)^2$  with minimal loss of fidelity. Considering the practical lower  $f\#$  limit of 1, the maximum error associated with this simplification is only  $\sim 11\%$  in the conservative direction of indicating lower SNR performance.\* With this simplification, the number of background photoelectrons becomes

$$e_b = \frac{\pi}{4} \cdot QE \cdot \tau \cdot L_b \cdot x^2 \cdot \left(\frac{d}{f}\right)^2 \cdot t, \quad [\text{photoelectrons}] \quad (12)$$

or

$$e_b = QE \cdot \tau \cdot L_b \cdot A \cdot \mu^2 \cdot t \quad [\text{photoelectrons}] \quad (13)$$

where  $A$  is the aperture area and  $\mu$  is the field of view of one detector pixel, or the instantaneous field of view (IFOV). In terms of optical system and detector variables,  $\mu$  is equal to pixel size divided by the focal length, or  $x/f$ .

### 3.3 Detection and Signal to Noise

The detection process is practically accomplished by applying a threshold to the individual digital counts for each pixel while accounting for known objects such as stars. Several approaches exist, to include sequential frame image subtraction whereby stationary objects are removed and moving objects remain. For the purposes here, we desire a means to accurately understand thresholds that provide detections with a low false alarm rate. Individual image frames consist of pixels containing noise from the background radiance, noise from internal detector sources and, when present, signals of interest (i.e., resident space objects). Intra-frame noise estimation can be accomplished by averaging the digital counts from a fraction of individual array pixels having the lowest values across the image.

The classical imaging signal to noise expression contains signal shot-noise as a noise component. This is important when considering spatially-extended image quality or accurate radiometry; however, this signal variance is not present in the background level pixels used for establishing a threshold to determine a detection event. The only noise components considered are the photoelectrons produced by the background Poisson-noise and the read noise from the detector ( $e_n$ ).† Therefore, the signal to noise expression for this application is

$$SNR = \frac{e_s}{\sqrt{e_b + e_n^2}}, \quad (14)$$

and provided in terms of photoelectrons. Given the relatively large pixel sizes (IFOV) of the optical systems of interest, the background radiance noise often dominates over that of the read noise. As will be seen, the detector read noise will limit the performance under circumstances when objects have a high angular rate and/or low background radiance.

Combining the expressions for the signal and background noise electrons (Equations 7 and 13, respectively) produces the signal to noise equation given by

$$SNR = \frac{QE \cdot \tau \cdot A \cdot \tau_{atm} \cdot E_{RSO} \cdot t_{sig}}{\sqrt{(QE \cdot \tau \cdot L_b \cdot A \cdot \mu^2 \cdot t) + e_n^2}}. \quad (15)$$

---

\* The 11% error is the difference in the square root of the background photoelectrons.

† Dark noise and other noise sources are negligible for modern detectors with the integration times of interest.

The scope of this effort is limited to detection via single pixel thresholding. An SNR threshold of six provides good detection performance with minimal false alarms. However, it is noted that additional processing algorithms can decrease the required SNR threshold and improve the performance by applying multiple imaging frames in the detection process, to include velocity-matched filters and median stacking techniques.<sup>18</sup> Furthermore, the advent of electron multiplying CCDs, or EMCCDs has enabled additional capabilities when the read noise ( $e_n$ ) is high relative to the background-generated photoelectrons ( $e_b$ ).<sup>19</sup> Finally, detection performance is not directly a function of the field of view (FOV) of the telescope. For uncued debris detection, a premium is placed on a large FOV, which drives the design to a fast optical system, typically  $f/1$  to  $f/2$ . This large FOV also results in multiple detection events as the object crosses the fixed FOV.

### 3.4 Optimized Signal to Noise

The signal integration time,  $t_{sig}$ , in Equation 15 is limited by the angular rate of the debris object, with the maximum time equal to the transit time through a single pixel on the detector with angular extent  $\mu$ . In terms of the variables above,  $\mu$  is the individual detector size,  $x$ , divided by the focal length,  $f$ . The maximum value of the signal integration time is then

$$Max(t_{sig}) = \frac{x}{f \cdot \omega}, \text{ [sec]} \quad (16)$$

where  $\omega$  is the object angular rate.

For cases where the background radiance dominates the detector read noise, the read noise term may be eliminated. Setting the read noise to zero, and substituting the maximum integration time for both  $t_{sig}$  and  $t$  in Equation 15 optimizes the SNR and results in

$$SNR = \sqrt{QE \cdot \tau \cdot A} \frac{\tau_{atm} \cdot E_{RSO}}{\sqrt{L_b \cdot \omega \cdot \mu}} \quad (17)$$

As for the optimized integration time required to achieve the performance of Equation 17, the angular rate of debris objects is not known *a priori*, but may only be approximated based on the sensing scenario of interest. Even when there is *a priori* knowledge of the debris angular rate, it will rarely be the case that the object transits exactly the length of a pixel during an exposure. Fractional elements of two or more pixels will typically be traversed depending on the relative starting position within a pixel and the direction. So for practical application, the optimized SNR equation suffers additional degradations due to the angular velocity uncertainties. However, Equation 17 provides the maximum theoretical performance which may be used to bound and understand various sensing systems and scenarios. A realistic degradation from this optimized condition may be approximated by degrading performance by  $\sqrt{2}$  assuming two pixel transits and another  $\sqrt{2}$  for the angular velocity uncertainty for a total optimized SNR degradation of a factor of two.

Each of the variables in the SNR equation may be independently grouped according to their association with the optical system, detector, atmosphere or debris object. These variables are summarized in Table 1.

It is important to remember the constraints and assumptions under which Equation 17 operates. The two primary conditions are that the square of the read noise must be small relative to the background-generated noise and the effective point spread function must be small relative to the pixel size on the focal plane. For uncued telescope survey systems of interest here, the background noise often dominates as the required short focal lengths for a large field of view results in a large single pixel angular extent, or IFOV. There are also additional system trades beyond detection performance which must be considered, such as the field of view, framing rate and positional (metric) accuracy. Although the governing equation infers performance improvements from decreasing the IFOV ( $\mu$ ), caution must be exercised, as the resulting decrease in background radiance per pixel can quickly be overcome by the read noise component.

The SNR equation is now explored for three scenarios: ground-based monitoring of the GEO regime, ground-based monitoring of LEO and GEO-based monitoring of GEO. For each of these cases, the applicable range of the variables of interest will be examined, and appropriate systems determined for effective debris monitoring. The predominant variable changes between the scenarios are the debris signature and angular rates ( $E_{RSO}$  and  $\omega$ ) and the atmospheric transmittance and background radiance ( $\tau_{atm}$  and  $L_b$ ).

Table 1 The detection signal to noise ratio equation variables.

Component	Description	Variable	Units
Optical System	Primary aperture area	$A$	$m^2$
	Focal length (IFOV component, $\mu = x/f$ )	$f$	m
	Net transmittance (to include obscurations)	$\tau$	-
Detector	Pixel pitch (IFOV component, $\mu = x/f$ )	$x$	m
	Quantum efficiency	$QE$	-
Resident Space Object (RSO)	RSO irradiance at telescope aperture	$E_{RSO}$	ph / $m^2$ / sec
	Object angular velocity	$\omega$	rad / sec
Atmosphere and/or Background	Background radiance	$L_b$	ph / sr / $m^2$ / sec
	Atmospheric transmittance	$\tau_{atm}$	-

#### 4. GROUND-BASED SENSING OF GEO

The first scenario is the commonly-used means of monitoring GEO objects from ground-based telescopes. Atmospheric transmittance is examined, along with the background radiance produced by the atmosphere (which is explicitly *foreground* radiance). The angular rate of GEO objects under this condition is summarized, and finally the system performance is analyzed.

##### 4.1 Atmosphere Transmittance for Ground-based Systems

From the governing equations, it is seen that the atmosphere drives two key variables, the atmospheric transmittance ( $\tau_{atm}$ ) and the background radiance ( $L_b$ ). As previously discussed, the spatial-resolution limitations imposed by the atmosphere are not of concern here. Atmospheric transmittance is influenced by several factors, to include aerosol and water vapor content, and the altitude of the observing site.

The atmospheric radiative propagation code MODTRAN<sup>20</sup> was used to generate the atmospheric properties for two cases of interest that bound the conditions which would be found at sites suitable for telescope placement. A “pristine” site is considered, having an altitude of 10,000 feet along with a “good” site at an altitude of 2,000 feet.<sup>‡</sup> The resulting zenith spectral transmittance is shown in Figure 2.

---

<sup>‡</sup> MODTRAN atmospheres used for these sites are “Sub Arctic Winter” for the 10,000 ft case and “U.S. Standard” for the 2,000 ft case. For both sites, 23 km visibility with rural extinction was used.

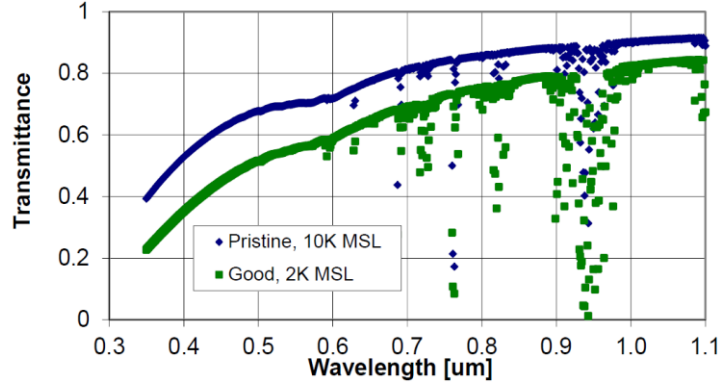


Figure 2 MODTRAN-generated spectral transmittance at zenith for a “good” and “pristine” telescope sites which are 2000 and 10,000 feet above sea level, respectively.

The atmospheric transmittance may be accurately modeled using the planar atmospheric assumption such that the atmospheric path length increases as the secant of the zenith angle. This approach accurately represents the transmittance under cloudless conditions down to elevation angles as low as  $5^\circ$  with minimal error. Given a zenith atmospheric transmittance of  $\tau_{atm0}$ , the transmittance as a function of elevation angle,  $\theta$ , is therefore

$$\tau_{atm} = \tau_{atm0}^{\sec(\pi/2-\theta)}. \quad (18)$$

The pristine site case, when considering the solar spectral irradiance and spectral response of a typical CCD provides a zenith transmittance of  $\tau_{atm0} = 0.8$ .

#### 4.2 Atmospheric Background Radiance

For ground-based sensing of GEO, it is assumed a “good” location is used such that the background radiance at zenith is on the order of  $19.5 \text{ m}_v/\text{asec}^2$  at nautical twilight (when the sun is  $12^\circ$  below the horizon) further decreasing to 20 to 21  $\text{m}_v/\text{asec}^2$  at astronomical twilight (or when the sun is  $18^\circ$  below the horizon). Sky brightness also increases with increasing zenith angle (or decreasing elevation angle). The same atmospheric scattering mechanisms responsible for decreased transmittance also serve to increase the total scattering. Examination of typical ground sites indicates the background radiance at an elevation angle of 30 degrees is 1.5 that of zenith, and further increases to a factor of 2 at an elevation angle of  $15^\circ$ . Figure 3 illustrates the typical increase in background radiance as a function of elevation angle. Localized light pollution such as that from distant cities may contribute additional radiance having a high azimuth dependency, particularly at low elevation angles.

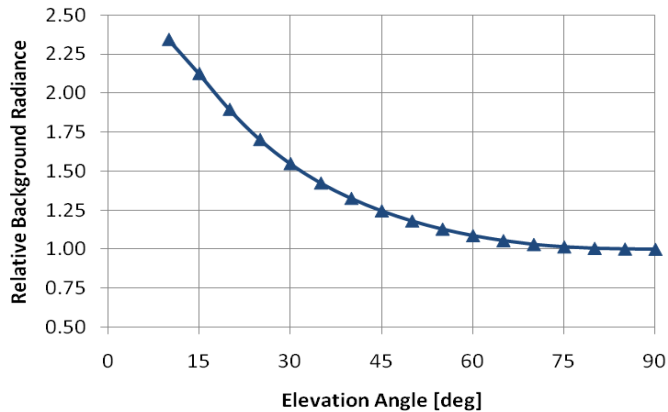


Figure 3 The relative background radiance levels from a ground-based site as a function of elevation angle.

To represent the elevation angle dependence of background radiance, a third-order polynomial was fit to the observed behavior from sites. The resulting background radiance as a function of elevation angle (in radians) is given according to

$$L_B(\theta) = L_{B0}(-0.6118 \cdot \theta^3 + 2.6249 \cdot \theta^2 - 3.8585 \cdot \theta + 2.9482), \quad (19)$$

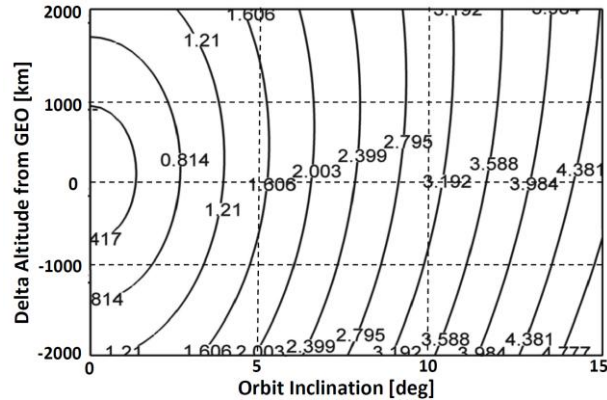
where  $L_{B0}$  is the zenith background radiance.

Background radiance during twilight conditions and will be of significant concern for the ground-based monitoring of LEO RSOs, and will be further discussed in Section 5.1.

### 4.3 GEO RSO Angular Rates from the Ground

A true geostationary satellite will have no motion relative to the ground. However, debris in the GEO regime does not maintain a stationary position, as the natural solar and lunar perturbations results in inclination growth over time, thus providing a north-south velocity component.<sup>21</sup> Furthermore, altitude differences such as objects in the GEO “disposal” orbit provide an east-west relative velocity component. A simple circular orbit will be considered to derive the angular velocities for this and subsequent scenarios.

RSOs with altitudes below the GEO belt will have higher orbital velocities, and therefore an eastward velocity relative to a stationary GEO position. Similarly, those with altitudes above GEO will have a relative westward motion. The north-south velocity due to inclination reaches a maximum as GEO objects cross zero declination, and reaches zero at the north-south “turn-around” points or when the declination equals the inclination. Deriving these individual angular velocity components and adding them in quadrature produces the relative angular rates of GEO RSOs as viewed from the ground. The angular rates as a function of semi-major axis (altitude) and inclination are shown in Figure 4, where it is seen that the angular rates of interest for this scenario are less than 5 asec/sec. Note the minor effects of varying elevation angles and site location latitude is not included.



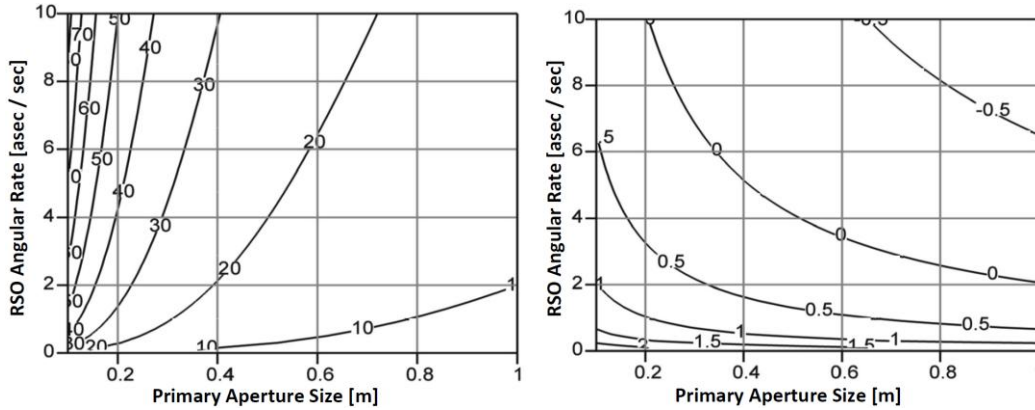


Figure 5 Performance of ground-based optical systems for detecting GEO objects. At left is the minimum detectable RSO size (in cm) as a function of the angular rate and the telescope aperture size. At right, is the log of the optimized integration time (in seconds) as a function of the same variables (with system parameters provided in the text).

In this example, it is important to note that the required assumptions to apply the optimized SNR equation hold, though at the 1.0 meter aperture size, the IFOV becomes comparable with typical atmospheric seeing conditions. The read noise has a negligible effect due to the higher background-generated photoelectrons.

The widely reported and successful operation of the ISON network provides a specific example of the effective use of small aperture wide-field systems used in a survey mode. The reported performance of these systems<sup>22,23</sup> is consistent with the model results. Although larger apertures enable greater detection capabilities, they also come at the price of reducing the field of view of the system. Figure 6 illustrates the FOV and IFOV for the  $f/\#$  1.2 system as a function of aperture size, while using a large-format 36 mm CCD having a 12  $\mu\text{m}$  pitch.

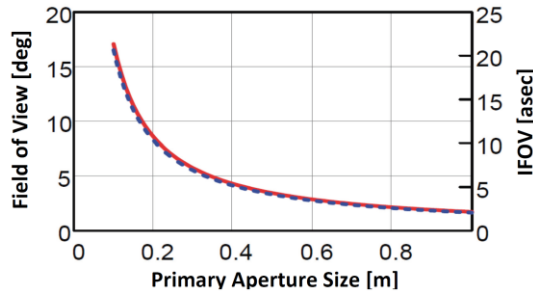


Figure 6 The field of view (left y-axis) and instantaneous field of view (right y-axis) as a function of aperture size for an  $f/\#$  1.2 optical system with a 36 mm CCD having 12  $\mu\text{m}$  pixels.

## 5. GROUND-BASED SENSING OF LEO

Radar systems have long been the sensor of choice for monitoring the LEO environment. The ability to conduct debris measurements independent of weather or lighting conditions favors their use. However, new classes of optical instruments, largely pioneered by the astronomical community with an objective of characterizing transient events such as gamma ray bursts and extra-solar system planetary transits<sup>24,25,26,27</sup> has demonstrated the potential to provide high-volume monitoring of orbital debris, enabled by very large fields of view (typically greater than five degrees per aperture). These wide field astronomical instruments typically have long integration times which are not optimized for detecting high angular rate LEO debris (nor are they intended to), resulting in degraded detection performance (per Section 3.4). Optimizing the integration time of these systems enables significant performance for debris monitoring.

### 5.1 Background Radiance & Terminator Conditions

The “dark sky” background radiance behavior, or when the sun is  $12^\circ$  or lower below the horizon, was covered in Section 4.2 for analyzing GEO monitoring. For LEO RSO monitoring, the requirement for a dark ground site and solar

illuminated space objects (or terminator conditions) restricts times and geometries over which they may be observed. The darkening twilight sky favorable for detection performance comes at the expense of an increasing earth umbra height such that the eligible volume of space for illuminated RSOs is decreased. For this reason, it is necessary to analyze the performance of these systems under twilight as well as darker conditions.

For solar declination angles less than  $12^\circ$ , the sky background rapidly increases and obviously becomes highly azimuthally asymmetric, with the brightest region at the horizon above the subsolar point. At sunset, a typical zenith sky brightness is around  $7.5 \text{ m}_v/\text{asec}^2$ , decreasing to  $\sim 13.5, 16.5$  and  $19.5 \text{ m}_v/\text{asec}^2$  at solar declination angles of  $6^\circ, 9^\circ$  and  $12^\circ$ , respectively.<sup>28</sup> Observing a sunset also attests to the varying spectral content of the twilight sky, though this is not addressed in detail here.

There are perceptions of significantly limited RSO visibility due to the terminator lighting condition requirement. However, recent analysis demonstrates significant coverage as a function of varying site latitudes and seasons. For instance, a site located at  $45^\circ$  degrees north maintains some visibility to illuminated LEO debris objects throughout the night during summer. Also, operating these systems at lower elevation angles dramatically increases the LEO orbit intersection volume—approximately 90% of debris object passes occur at elevation angles less than 50 degrees.<sup>29</sup>

### 5.2 Ground to LEO RSO Angular Rates

Lower altitude LEO objects may exceed angular rates of one degree per second relative to a ground observer when viewed at high elevation angles. However, as previously discussed, telescope pointing at lower elevation angles are preferred, as the volume of objects dramatically increases. At an elevation angle of  $\sim 30^\circ$ , the typical angular rate of LEO objects are  $\sim 1000 \text{ asec}/\text{sec}$  or  $\sim 0.25 \text{ deg}/\text{sec}$ . Figure 7 illustrates a range of angular rates associated with LEO objects as a function of elevation angle and orbital altitude.

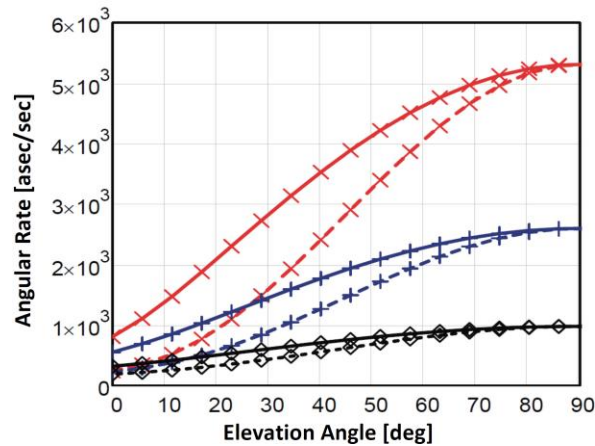


Figure 7 A range of LEO RSO angular velocities as seen from the ground are shown as a function of elevation angle. Circular orbit altitudes of 300 km (X), 600 km (+) and 1500 km ( $\diamond$ ) are provided, with solid lines representing the maximum angular velocity, and the dotted lines the minimum.

### 5.3 Performance of Ground-based Systems for LEO

Now, we'll investigate the performance of ground-based systems for LEO. For this example, an orbital altitude of 800 km is chosen, or one with a high spatial density of cataloged debris.<sup>30</sup> At a  $30^\circ$  elevation angle, this altitude corresponds to a range of 1395 km. The same system variables are maintained as with the preceding GEO example, with the exception of the pixel size that has been doubled to  $24 \mu\text{m}$ . However, now the angular rates of interest are significantly higher. The performance results are shown in Figure 8.

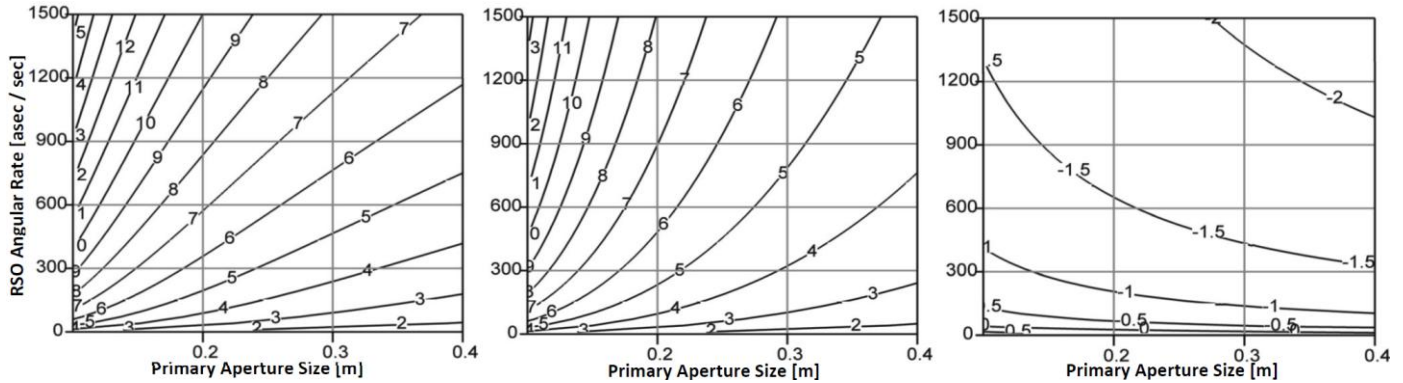


Figure 8 Performance of ground-based optical systems for detecting LEO objects in an 800 km orbit with the telescope at a 30° elevation angle. At left is the minimum detectable RSO size (in cm) as a function of the RSO angular rate and the telescope aperture size given a read noise of  $8 e^-$ . In the middle is the theoretical performance limit, or that with no read noise. At right is the log of the optimized integration time (in seconds) as a function of the same variables.

Of particular interest is that aperture sizes less than 20 cm have detection capabilities for objects 10 cm and smaller, or below the nominal size of cataloged objects. Also, the resulting integration times are very short compared to typical standards: 20 ms for a 20 cm aperture optimized for a 1000 asec/sec object. The short integration times result in the read noise dominating over the background noise, as seen in comparing the actual the theoretical performance results in Figure 8. Mated with a large format CCD, the 20 cm telescope of this design provides a 10° FOV with a ~20 asec IFOV.

Given the additional terminator opportunities provided by twilight operation, the detection thresholds for the same system but with background levels of  $16.5 m_v/asec^2$ ,  $13.5 m_v/asec^2$  and  $10.5 m_v/asec^2$  (approximately corresponding to solar declination angles of 9°, 6° and 3°) are shown in Figure 9. Under these circumstances, the  $8 e^-$  of read noise becomes negligible due to the high background levels.

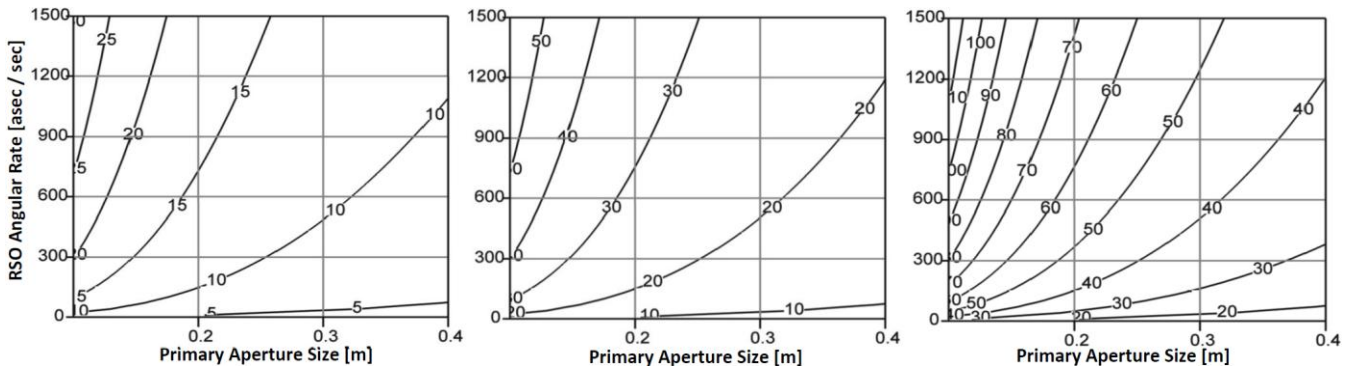


Figure 9 Performance of the system as illustrated in Figure 8, but with twilight background radiance conditions of  $16.5 m_v/asec^2$  (left),  $13.5 m_v/asec^2$  (middle) and  $10.5 m_v/asec^2$  (right).

As illustrated by Figure 9, these systems provide meaningful twilight condition performance. Further improvements are enabled by reducing the 24  $\mu m$  pixel size along with the corresponding decrease in integration time. This performance improvement is possible since the background radiance dominates over the read noise.

Finally, some closing observations are made on the elevation-angle performance dependency. As previously mentioned, operating at a lower elevation angle significantly improves the RSO volume transiting the field of view of the system. This improved volume comes at the expense of the increased range and hence reduced signal. However, the lower angular rate of LEO objects at lower elevation angles buys back some of these performance impacts. Figure 10 illustrates the relative effects.

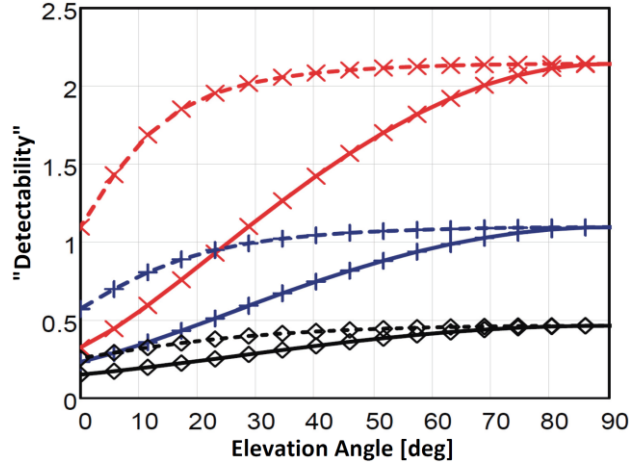


Figure 10 The “detectability” of LEO objects normalized relative to an RSO at 600 km with a 30 degree elevation angle. Orbits of 300 km (X), 600 km (+) and 1500 km (◇) are shown. Solid lines represent the highest angular rates, while the dashed lines are the smallest (following that of Figure 7). Note this does not include atmospheric effects.

Given the anticipated system performance, there is significant potential to contribute to LEO debris surveillance as a complementary approach to radars. Multiple apertures enable very large fields of view, providing high-volume and cost-effective coverage. Proper latitude placement extends the required terminator lighting conditions, while multiple sites mitigate weather impacts. Although the RSO ranges are not directly determined, the metric position accuracies would exceed that of most radar systems.

## 6. GEO-BASED SENSING OF GEO

The next case of interest is observation of GEO debris from optical systems hosted in GEO, such as on a communications satellite. This approach is attractive, as the distances from the ground to GEO challenge ground-based sensor performance. In-situ GEO sensing with optical sensors could provide a means to improve understanding of the GEO environment, and guide subsequent debris mitigation practices.

For space-based sensors, the background radiance is a function of the observation direction relative to the solar ecliptic plane, which provides scattering from intra-solar system dust as a function of solar phase angle. There is also a dependence upon the galactic plane, where high stellar densities are responsible for the background radiance contributions. The background radiance is treated as spatially uniform on a scale of multiple pixels. For space-based sensors, a typical background is  $22 \text{ m}_v/\text{asec}^2$ , and this will be used in the model to assess performance. Also, unlike ground-based systems, there is no naturally-imposed minimum range to debris, which in turn results in very high angular rates for close-in objects.

### 6.1 GEO to GEO RSO Angular Rates

The angular rates of GEO objects as seen from a station-kept GEO platform are investigated as an input to the governing SNR equation. For our example investigation, the discussion will be limited to angular rates presented by objects with circular orbits and at the GEO plane crossing, or at zero declination. The absolute “north-south” velocities are dominated by the object orbital inclination, while the “east-west” relative velocities are driven by differences in the orbital altitude. A maximum orbital inclination of  $15^\circ$  is considered, or around the highest achieved due to the natural solar-lunar gravitational perturbations for typical area-to-mass ratio objects. The distances of interest may extend to several degrees away in GEO, but this analysis emphasizes shorter ranges of one degree or less in longitude, equivalent to  $\sim 736 \text{ km}$ .

The angular rates are determined by calculating the absolute “north-south” velocities and adding them in quadrature to the “east-west” velocities relative to a true GEO orbit. Having obtained the total velocity component orthogonal to the sensor, this is divided by the object range. The range was determined as a function of GEO belt angle and altitude difference, with the results shown in Figure 11. The angular rates for GEO altitude objects with varying inclination and ranges are shown in Figure 12.

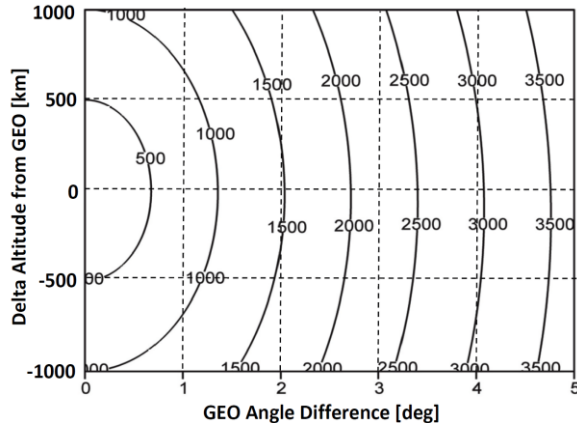


Figure 11 The range (in km) to other GEO positions as a function of the difference in the GEO belt angle (x axis) and altitude difference (y axis).

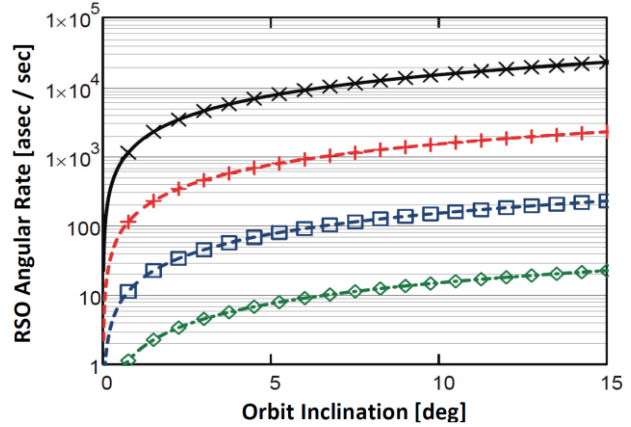


Figure 12 The angular rates of GEO RSOs crossing zero declination as a function of orbital inclination (x axis). Rates are shown for objects having GEO angle differences of  $0.01^\circ$  (X),  $0.1^\circ$  (+),  $1^\circ$  ( $\square$ ) and  $10^\circ$  ( $\diamond$ ).

The angular rate of GEO objects at the plane crossing is given as a function of both their orbital inclination and altitude difference for three ranges of interest (longitude differences of  $0.01^\circ$ ,  $0.1^\circ$  and  $1.0^\circ$ ) which will be used for the sensor performance analysis (Figure 13).

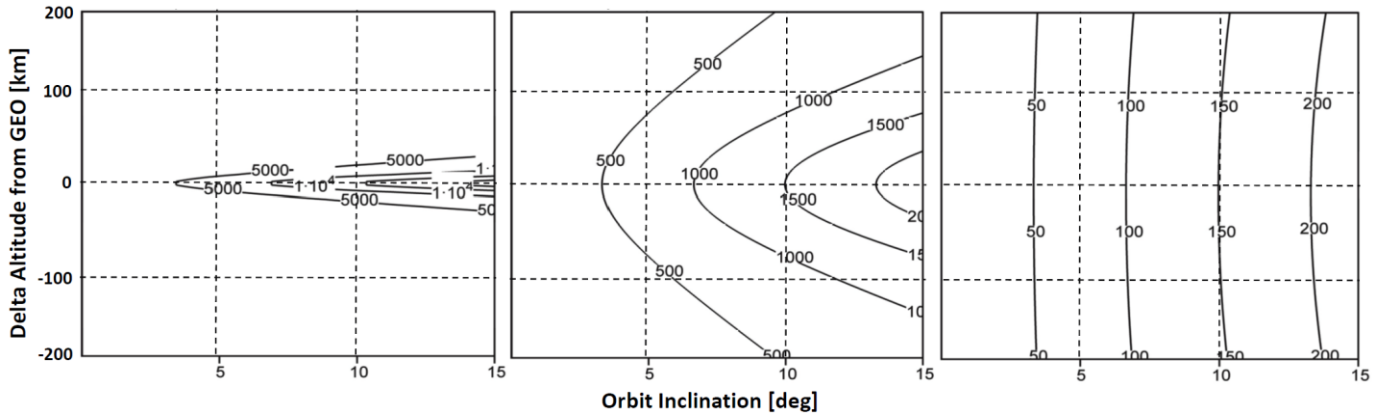


Figure 13 A range of angular rates of GEO objects (in units of asec/sec) as a function of orbital inclination (x-axis) and altitude difference from GEO (y-axis). From left to right are GEO angle differences of  $0.01^\circ$ ,  $0.1^\circ$  and  $1^\circ$ .

## 6.2 Performance of GEO-based Systems for GEO

With the angular rates of interest determined, GEO-based sensing performance is examined. Ranges corresponding to GEO angle differences of  $0.01^\circ$ ,  $0.1^\circ$  and  $1^\circ$  are investigated; or 7.36 km, 73.6 km and 736 km; respectively. As shown in Figure 13, the corresponding maximum angular rates for  $15^\circ$  inclined objects are 25000 asec/sec, 2500 asec/sec and 250 asec/sec. The performance analysis spans aperture sizes from 1 cm to 10 cm, or those which would minimize host vehicle impact as a secondary mission. The other system parameters are set as with the previous examples, with the only changes consisting of the lower background radiance ( $L_B = 22 \text{ m}_v/\text{asec}^2$ ) and no atmospheric transmittance penalty due to space-based sensing, and the use of  $24 \mu\text{m}$  pixels. As a reminder, the remaining system parameters include:  $f/\#$  of 1.2,  $\tau = 0.6$ ,  $\tau_{am} = 1$ ,  $QE = 0.7$ ,  $e_n = 8 e^-$ ,  $\psi = 90$  and  $\rho = 0.2$  (equally divided among diffuse and specular components). The performance results are shown in Figure 14.

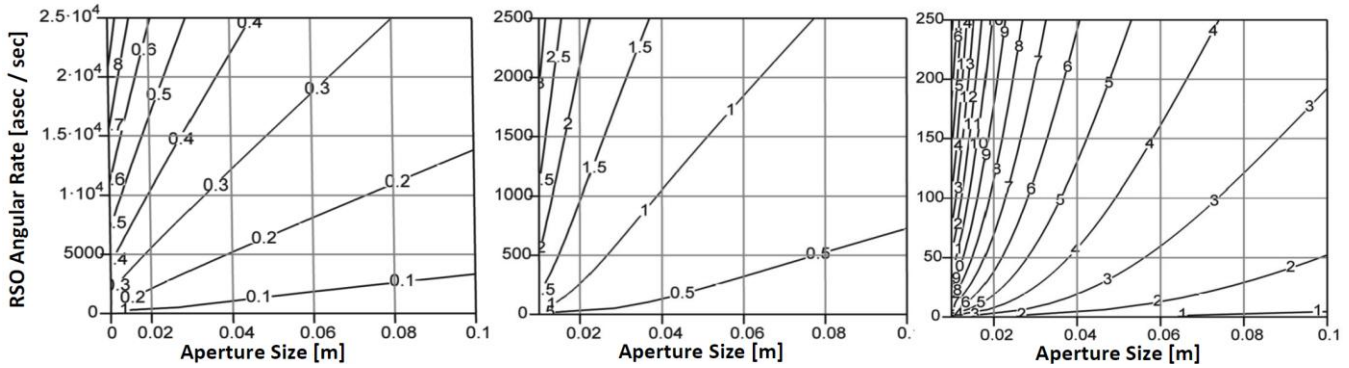


Figure 14 Performance of GEO-based sensors at three ranges and corresponding span of angular rates. The minimum detected object size (in cm) as a function of aperture size and angular rate is presented. From left to right are ranges of 7.36 km, 73.6 km and 736 km, or GEO belt angle differences of  $0.01^\circ$ ,  $0.1^\circ$  and  $1^\circ$ .

Performance for the closest two ranges in Figure 14 are limited by the read noise, while detection of longer-range objects  $1^\circ$  away in the GEO belt is background-limited. Of significance is the capability for these small aperture systems to detect small GEO debris. Aperture sizes of only 2 cm can provide sub 10 cm detection performance at ranges up to  $1^\circ$  away. Their use could significantly add to the understanding of the GEO debris environment, particularly the spatial densities for objects in the 1 mm to 10 cm size class. Hosting these sensors on platforms such as communication satellites could provide a cost-effective means of monitoring GEO debris.<sup>31</sup> Alternatively, dual use components such as star trackers could be adapted for this mission role.

## 7. FROM DETECTION TO UTILITY

Detection of orbital debris in and of itself is only useful for statistically characterizing the debris population. Ultimately, maintenance of debris objects in a catalog is desired, with updates of sufficient frequency such that mission impacts from potential collisions may be mitigated. Furthermore, positional accuracy improvements enabled by more frequent monitoring minimize the error associated with conjunction events, thus reducing the required collision avoidance maneuvers. This is particularly true for the congested LEO orbit, where uncertain atmospheric drag effects impact the orbit propagation fidelity.

Beyond detection, three quantities are required to develop and refine orbital parameters of debris objects: the sensor position, the time of the measurement, and the position of the debris object being observed, where “position” is the angles-only position as referenced by the stellar background. By mapping the known stellar background positions to the focal plane, accurate absolute positions may be determined at the sub-pixel level. The position accuracy is interdependent with the detection performance of optical systems emphasized in this work, as it directly correlates to the field of view of a single pixel, or IFOV of the system.

For the wide field, ground-based systems monitoring LEO, further work is required to better understand how they may be used to provide an initial orbit solution such that subsequent correlations required to generate quality orbital parameters are obtained.<sup>32</sup> At a minimum, these systems should be able to provide updates to the orbits of existing objects. Although a metric accuracy of 10 asec is usually considered poor under the typical circumstances of observing GEO objects, this translates into distances of  $\sim 27$  m to 83 m for LEO orbits when viewed at a  $30^\circ$  elevation angle and spanning orbit altitudes from 300 km to 1000 km.

The GEO-based sensors seem suitable for statistical characterization of the debris environment, with sensitivity maximized if a wide range of integration times are used corresponding to the wide variability of angular rates experienced. Hosting these small sensors on a GEO-stationary platform would seem a cost-effective approach. Orbit determination of debris using these sensors alone is likely challenging; however, observation of larger debris objects coupled with ground-based systems of sufficient sensitivity could yield meaningful improvements due to the roughly orthogonal viewing positions which resolve the range ambiguity.

## 8. CONCLUSIONS

Commercial advances in optical system design, detector technology, and computational capabilities have enabled significant performance from telescopes to monitor orbital debris. The performance estimates from these systems have been determined in terms of the inferred debris sizes, resulting from their signature estimates. The governing radiometric equation was developed illustrating the performance dependencies as a function of the optical system, the background radiance, the atmosphere and the angular rate of the debris objects. High-angular rate objects result in optimized integration times which are very short, leading to cases where the read noise may dominate performance over the background radiance.

The relatively new approach of broad area LEO surveillance from small aperture ground-based systems appears to hold significant promise. These systems should provide a cost-effective means of updating existing debris object orbital parameters. GEO-based cameras, to include dual-use star trackers, may provide significant detection performance, in particular if a wide range of integration times are possible. Improved understanding of the small GEO debris population is needed to further manage GEO disposal practices and the long-term potential degradation of satellite materials which may be contributing to this population.

*Disclaimer: The views expressed in this document are those of the author and do not reflect the official policy or position of the U. S. Air Force, Department of Defense, or the U. S. Government.*

## 9. REFERENCES

- 
- [1] J. -C. Liou, editor, "Update on Three Major Debris Clouds," *Orbital Debris Quarterly News*, 14(2), April 2010, [www.orbitaldebris.jsc.nasa.gov](http://www.orbitaldebris.jsc.nasa.gov).
  - [2] Nicholas L. Johnson, "Orbital Debris: The Growing Threat to Space Operations," *33rd Annual AAS Guidance and Control Conference*, February 6-10, 2009, AAS 10-011.
  - [3] Paula H. Krisko, Yu-Lin Xu, K. Abercromby and Mark Matney, "The Geosynchronous Environment for ORDEM2010," 60th IAC (International Astronautical Congress), 12-16 Oct. 2009, Report #: JSC-CN-18954; JSC-CN-18984
  - [4] R. Sridharan and Antonio F. Pensa, "U.S. Space Surveillance Network Capabilities," in *Characteristics and Consequences of Space Debris and Near-Earth Objects*, Proc. SPIE 3434, 88-100, (1998).
  - [5] Statement by US State Department, Maj Gen Susan Helms, USAF Director of Plans and Policy, United States Strategic Command Remarks to United Nations Committee on the Peaceful Uses of Outer Space (UNCOPUOS), Vienna 10 Jun 2010.
  - [6] *Handbook for Limiting Orbital Debris*, NASA Handbook 8719.14, approved July 30, 2008.
  - [7] "National Space Policy of the United States of America," June 28, 2010, available via <http://www.whitehouse.gov>
  - [8] United Nations Committee on the Peaceful Uses of Outer Space, "Report of the Scientific and Technical Subcommittee on its forty-seventh session, held in Vienna from 8 to 19 February 2010," AC.105/958, 11 March 2010.
  - [9] C. L. Stokely, J. L. Jr. Foster, E. G. Stansbery, J. R. Benbrook, and Q. Juarez, "Haystack and HAX Radar Measurements of the Orbital Debris Environment--2003," JSC-62815, 2006.
  - [10] Gene Stansbery, J.-C. Liou, M. Mulrooney, and M. Horstman, "Current and Near-Term Future Measurements of the Orbital Debris Environment at NASA," *33rd Annual AAS Guidance and Control Conference*, February 6-10, 2009, AAS 10-013.
  - [11] R. Lambour, N. Rajan, T. Morgan, I. Kupiec and E. Stansbery, "Assessment of Orbital Debris Size Estimation from Radar Cross Section Measurements," *Advances in Space Research*, vol. 34, no. 5, pp. 1013-1020, 2004.
  - [12] Lambert, J. V., Osteen, T. J. and Kraszewski, W. A. "Determination of debris albedo from visible and infrared brightness," in *Space Debris Detection and Mitigation*, Proc. SPIE 1951, 32-36, (1993).

- 
- [13] Mark K. Mulrooney, Mark J. Matney, Matthew D. Hejduk, and Edwin S. Barker, "An Investigation of Global Albedo Values," in *Advanced Maui Optical and Space Surveillance Technologies Conference*, 2008, pp. 624-633.
- [14] A. E. Potter, "Ground-based Optical Observations of Orbital Debris: A Review," *Adv. Space Res.*, vol. 16, no. 11, pp. 35-45, 1995.
- [15] F. E. Nicodemus, J. C. Richmond, J. J. Hsia, I. W. Ginsburg, and T. Limperis, "Geometrical Considerations and Nomenclature for Reflectance," NBS Monograph 160, 1977.
- [16] William E. Krag, "Visible Magnitude of Typical Satellites in Synchronous Orbits," Massachusetts Institute of Technology, September 6, 1974, ESD-TR-74-278.
- [17] John R. Schott, "Remote Sensing: The Image Chain Approach," Oxford University Press, 1997.
- [18] Toshifumi Yanagisawa, Hirohisa Kurosaki and Atsushi Nakajima, "Present Status of Space Debris Optical Observational Facility of JAXA at Mt. Nyukasa," *Proceedings of the Fifth European Conference on Space Debris*, ESA SP-672, July 2009.
- [19] Alejandro Ferrero, et al., "Electron-multiplying CCD Astronomical Photometry," *Sensors, Cameras, and Systems for Industrial/Scientific Applications XI*, SPIE/IS&T Vol. 7536, 2010.
- [20] Alexander Berk, Lawrence S. Bernstein, and David C. Robertson. "MODTRAN: A moderate resolution model for LOWTRAN 7," Technical Report GL-TR-89-C122, Air Force Geophysics Lab, April 1989.
- [21] S. H. Vaughan and T. L. Mullikin, "Long Term Behavior of Inactive Satellites and Debris Near Geosynchronous Orbits," AIAA 95-200, AAS/AIAA Spaceflight Mechanics Meeting, Albuquerque, NM, 1995.
- [22] Vladimir Agapov, Igor Molotov and Zakhary Khutorovsky, "Analysis of Situation in GEO Protected Region," *Advanced Maui Optical and Space Surveillance Technologies Conference*, 2009, pp. 180-189.
- [23] I. Molotov, V. Agapov, et al., "ISON Worldwide Scientific Optical Network," *Proceedings of the Fifth European Conference on Space Debris*, ESA SP-672, July 2009.
- [24] Katarzyna Malek, et al., "General overview of the 'Pi of the Sky' system," in *Photonics Applications in Astronomy, Communications, Industry, and High-Energy Physics Experiments*, Proc. SPIE 7502, (2009).
- [25] Roman Wawrzaszek, et al., "Possible use of the 'Pi of the Sky' system in a Space Situational Awareness program," in *Photonics Applications in Astronomy, Communications, Industry, and High-Energy Physics Experiments*, Proc. SPIE 7502, (2009).
- [26] Grigory Beskin, et al., "From TORTORA to MegaTORTORA—Results and Prospects of Search for Fast Optical Transients," *Advances in Astronomy*, Volume 2010, Article ID 171569.
- [27] D. L. Pollacco, et al., "The WASP Project and the SuperWASP Cameras," *Publications of the Astronomical Society of the Pacific*, Vol 118, pp. 1407-1418, 2006.
- [28] Bradley E. Schaefer, "To the Visual Limits," *Sky and Telescope*, May 1998, Vol 95, Issue 5.
- [29] Vasilii S. Yurasov and Viktor D. Shargorodskiy, "Features of Space Debris Survey in LEO Utilizing Optical Sensors," *Proceedings of the Fifth European Conference on Space Debris*, ESA SP-672, July 2009.
- [30] J. -C. Liou, editor, Graphic: "Current Debris Environment in Low Earth Orbit," *Orbital Debris Quarterly News*, 13(3), July 2009, [www.orbitaldebris.jsc.nasa.gov](http://www.orbitaldebris.jsc.nasa.gov).
- [31] Timothy L. Deaver, "Leveraging Commercial Communication Satellites to support the Space Situational Awareness Mission Area," in *Advanced Maui Optical and Space Surveillance Technologies Conference*, 2008, pp. 69-74.
- [32] K. T. Alfriend, C. Sabol and J. Tombasco, "Orbit Determination and Prediction for Low Earth Orbit Satellites Using A Single Pass Of Observation Data," Paper No. AAS 07-121, *2007 AAS/AIAA Space Flight Mechanics Conference*, Sedona, AZ, 28 Jan. - 1 Feb. 2007.